Journal of the Brazilian Society of Mechanical Sciences and Engineering (2024) 46:280
https://doi.org/10.1007/s40430-024-04843-9

TECHNICAL PAPER

A two-dimensional boundary layer model for combustion chamber simulation

Erykson M. S. Costa[1] · Marcio T. Mendonca[1] · Fernando S. Costa[1] · Cesar A. V. Salvador[2]

Received: 17 June 2022 / Accepted: 3 November 2023

Abstract

Different propulsion systems can be used for launching payloads into orbit and for attitude control, orbit correction and maneuvering of satellites. Liquid bipropellant thrusters are used in applications requiring high specific impulses and high thrust levels and numerical simulation models can reduce development costs and time. This work describes a new 2D numerical model based on the boundary layer equations for the simulation of spray combustion. This model can be applied to the preliminary design of rocket combustion chambers, and allows the determination of droplet vaporization lengths, chemical composition, temperature profile and other thermodynamic and propulsion parameters. The computation time is, in general, lower than more complex 2D and 3D simulation models. Liquid fuel and oxidizer are injected into the combustion chamber with known droplet sizes and a pre-existing gas flow, which represents combustion products recirculation. The governing equations are discretized using centered and backward finite differences and the solution is marched downstream, considering droplet evaporation, mixture and combustion of propellant vapors with pre-existing gases. Burning of unsymmetrical dimethylhydrazine (UDMH) and dinitrogen tetroxide (NTO) was simulated with different mixture conditions and taking into account eleven product species. The model was validated by considering separately the different routines, comparing results of internal boundary layer flows, droplet evaporation and combustion products composition against expected theoretical behavior and results from other models. The influence of the equivalence ratio radial distribution on flow parameters was evaluated. The gas temperatures near the wall remained relatively constant after a certain distance downstream, depending on the local equivalence ratio distribution. The boundary layer remained very thin along the chamber due to the constant addition of combustion products.

Keywords Propulsion · Combustion chamber · Reactive flow · Boundary layer · Two phase combustion · Combustion chamber cooling

1 Introduction

Mathematical models for spray combustion are important for the development of combustion chambers since they allow comparative analysis of conditions and chamber configuration, reducing the number of test, development time and costs. Numerical and analytic models can be zero, one, two or three-dimensional and can be steady or transient. In 1998, the complexities associated with modeling high-pressure mixing and combustion in rocket engines have been highlighted by [12]. The problems raised by nonlinear source terms in the balance equations, turbulence modeling, scalar mixing and real gas effects at high pressure were discussed and available modeling options at the time were presented. Simulation performance and accuracy aspects were discussed.

Technical Editor: Mario Eduardo Santos Martins.

✉ Marcio T. Mendonca
marcio_tm@yahoo.com

Erykson M. S. Costa
ErycksonMarconny@gmail.com

Fernando S. Costa
fernando.costa@inpe.br

Cesar A. V. Salvador
valverde@ufsm.br

[1] Instituto Nacional de Pesquisas Espaciais, São José dos Campos, Brazil

[2] Universidade Federal de Santa Maria, Santa Maria, Brazil

Published online: 05 April 2024

A well-known zero dimensional model is the NASA Chemical Equilibrium Applications program (CEA-NASA 2004 https://cearun.grc.nasa.gov/) that calculates composition of combustion products, flame temperature, transport properties, thermodynamic and propulsion parameters. One example of a one-dimensional model is the work of [16] who presented a model for the simulation of spray combustion in rocket chambers and determined vaporization lengths of hydrazine and hydrazine mixtures. Zero dimensional and one-dimensional models do not allow for radial variation of parameters and, compared to these simple models, nowadays more complex and computationally demanding models based on computational fluid dynamics are available.

The German Center for Aerospace organized a workshop aiming at the evaluation of CFD tools for simulation of spray combustion [3]. The results presented at the workshop and the provided test configurations were used latter by other investigators to access their models. For example, [1] used those results to evaluate a multiphase, real fluid combustion model that was incorporated into a computational fluid dynamic model.

Numerical simulations of propulsion include also hybrid rocket engines. Among other works available in the literature the work of [10] may be given as an example of the initiatives in this direction. They proposed to develop an accurate combustion model to obtain temperature distribution, axial velocity, mass fraction distribution, as well as regression rates. Their model consists of CFD turbulent simulation of the balance equations using a partially stirred reactor model. A similar model based on open source software was developed by [9].

Other initiatives use commercial and in house CFD models coupled with multidisciplinary models in order to study thrust chamber cooling, including radiation and convection on both the combustor side and on regenerative cooling passages [5]. These models may also include injector geometry details as well as droplet motion, heat transfer, evaporation and breakup using Lagrangian formulation [4, 19]. Large eddy simulations for turbulent combustion and genetic algorithms couple with data base and reduced order models are also current practice [14, 15, 17].

In spite of remarkable advances in computational fluid dynamics of reactive flows, there are not many recent simple and fast two-dimensional models described in the literature for simulation of two phase flow combustion chambers. The use of simple and fast models are still relevant today for preliminary design of rocket engines combustion chambers and test bench planning. One-dimensional models are a first alternative to compute approximate averages of properties at each streamwise station of the combustion chamber in order to satisfy mass, momentum and energy balance. [16] used an one-dimensional model in order to compare the performance of hydrazine and hydrazine mixtures burning with nitrogen dinitrogen tetroxide in a multi-propellant combustion chamber. Two dimensional models are the next level of approximation and boundary layer equations may be used to develop such models [6]. These models allow a more detailed description of the reactive flow on the combustion chamber than one-dimensional models, taking into account radial gradients.

The objective of the present investigation is to present a two-dimensional model, extending the work of [16] by implementing boundary layer equations for the computation of the reactive flow through the combustion chamber. Mass, momentum and energy balance equations in two-dimensional control volumes at each streamwise section of the combustion chamber are solved. The model allows the study of radial variation of equivalence ratio, important for wall cooling methodologies. The proposed two-dimensional model considers the combustion process in the chamber controlled by the liquid fuel and oxidizer evaporation rate. The important parameters to be determined are the vaporization length, the wall temperature for different equivalence ratios in the wall region, the combustion products composition and radial velocity and temperature profiles.

This paper is organized in four sections: Sect. 1 presents an introduction to the problem; Sect. 2 describes the methodology, including verification and validation test cases; Sect. 3 presents results in terms of wall temperatures, gas composition, velocity and temperature profiles, droplet vaporization length and evolution of the fuel to oxidizer mass flow ratio along the chamber; Sect. 4 presents final comments and conclusions.

2 Methodology

Figure 1 shows a combustion chamber scheme where fuel and oxidizer are injected forming two sprays with known droplet size distributions. The propellants vaporize, burn and mix with pre-existing combustion products, raising the gas temperature inside the chamber. The fuel and oxidizer considered in this study are dimethylhydrazine (UDMH) and dinitrogen tetroxide (NTO). Propellants mixing and combustion are assumed to be much faster than evaporation, such that the resulting chemical composition is determined through a chemical equilibrium routine based on the balance of chemical components and equilibrium constants.

Mass, momentum and energy balance equations are solved, given initial conditions at the combustion chamber entrance. The following simplifying assumptions are considered:

1. two-dimensional axisymmetric, constant cross-sectional combustion chamber,
2. steady-state condition,

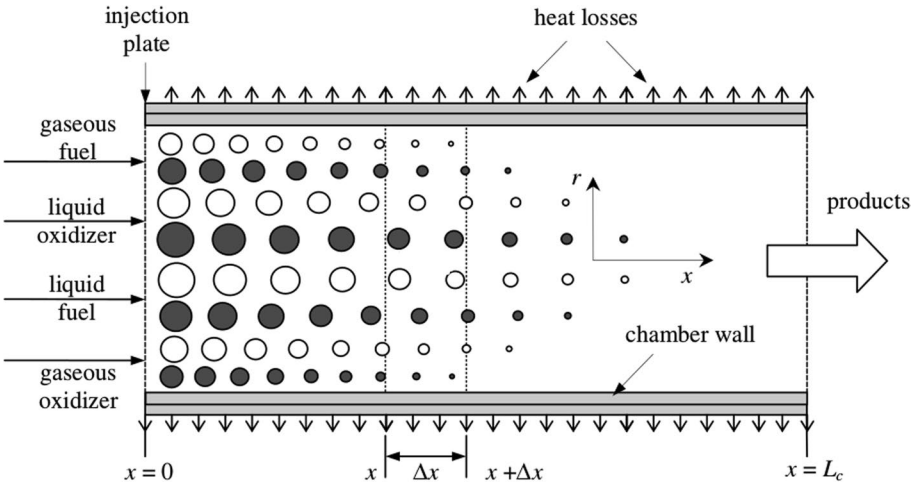

Fig. 1 Combustion chamber model [16]. L_c is the chamber length in the streamwise direction x and r is the radial direction

3. process controlled by vaporization of droplets,
4. no volume forces, such as gravity forces,
5. Soret and Dufour effects negligible,
6. negligible viscous dissipation,
7. no mass diffusion between neighbor volumes in the radial direction,
8. negligible radial pressure gradient,
9. heat, mass and momentum diffusion in the streamwise direction negligible, leading to boundary layer type equations.

2.1 Chemical equilibrium

The products composition is determined based on the method of constants of equilibrium, according to the following equations, where 11 species are present.

$$\begin{aligned} &C_x\,H_y\,O_z\,N_t + a\left(\,O_p\,N_q\right) \quad \rightarrow \\ &\quad n_{CO_2}\,C\,O_2 + n_{CO}CO + n_{H_2O}H_2O + n_{H_2}H_2 \\ &\qquad + n_{O_2}O_2 + n_{N_2}N_2 + n_H H + n_{OH}OH \\ &\qquad + n_O O + n_{NO}NO + n_N N. \end{aligned}$$

Where n stands for the number of moles of each species. This reaction leads to four balance equations for carbon, hydrogen, oxygen and nitrogen. Another seven equations are given by the equilibrium constants.

$$\frac{1}{2}H_2 \iff H, \qquad K_1 = \frac{X_H}{X_{H_2}^{1/2}}P^{1/2},$$

$$\frac{1}{2}O_2 \iff O, \qquad K_2 = \frac{X_O}{X_{O_2}^{1/2}}P^{1/2},$$

$$\frac{1}{2}N_2 \iff N, \qquad K_3 = \frac{X_N}{X_{N_2}^{1/2}}P^{1/2},$$

$$\frac{1}{2}H_2 + \frac{1}{2}O_2 \iff OH, \qquad K_4 = \frac{X_{OH}}{\left(X_{H_2}X_{O_2}\right)^{1/2}},$$

$$\frac{1}{2}N_2 + \frac{1}{2}O_2 \iff NO, \qquad K_5 = \frac{X_{NO}}{\left(X_{N_2}X_{O_2}\right)^{1/2}},$$

$$H_2 + \frac{1}{2}O_2 \iff H_2O, \qquad K_6 = \frac{X_{H_2O}}{X_{H_2}X_{O_2}^{1/2}}P^{-1/2},$$

$$CO_2 + \frac{1}{2}O_2 \iff CO_2, \qquad K_7 = \frac{X_{CO_2}}{XCOX_{O_2}^{1/2}}P^{-1/2}.$$

One additional equation is given by

$$\sum_{i=1}^{11} X_i = 1.$$

Where X stands for the mole fraction of each species.

2.2 Balance equations

Considering that the balance equations may be simplified with boundary layer approximation, the following equations in two-dimensional, axisymmetric cylindrical coordinates, result [6].

Continuity equation

$$\frac{1}{r}\frac{\partial}{\partial r}\left(\rho r u_r\right) + \frac{\partial}{\partial z}\left(\rho u_z\right) = 0. \tag{1}$$

Where, r and z are the radial and axial coordinates, ρ is the density, u_r and u_z are the radial and streamwise velocity components.

Streamwise and radial momentum equations

$$\rho u_r \frac{\partial u_z}{\partial r} + \rho u_z \frac{\partial u_z}{\partial z} = -\frac{\partial p}{\partial z} + \frac{1}{r}\frac{\partial}{\partial r}\left(r\mu \frac{\partial u_z}{\partial r}\right), \tag{2}$$

$$\frac{\partial p}{\partial r} = 0. \tag{3}$$

Where p is the pressure and μ stands for the dynamic viscosity coefficient.

Energy balance equation

$$\rho c_p \left(u_r \frac{\partial T}{\partial r} + u_z \frac{\partial T}{\partial z}\right) - u_z \frac{\partial p}{\partial z} = \frac{1}{r}\frac{\partial}{\partial r}\left(kr\frac{\partial T}{\partial r}\right). \tag{4}$$

Where c_p is the specific heat at constant pressure, k is the thermal conductivity coefficient and T stands for temperature.

Perfect gas equation of state

$$p = \rho R_u T \sum_{i=1}^{N} \frac{Y_i}{W_i}. \tag{5}$$

Where R_u is the universal gas constant, Y_i and W_i are the mass fraction and molar mass of species i.

$$X_i = \frac{Y_i/W_i}{\sum_j \left(Y_j/W_j\right)}. \tag{6}$$

Where X_i is the mole fraction of species i

2.3 Initial and boundary conditions

The above boundary layer equations are parabolic equations where information propagates downstream from given initial conditions. In the radial direction, boundary conditions are imposed at the combustion chamber centerline and at the wall.

The initial conditions are given at the injection plate combustion chamber entrance as shown in Fig. 1. Liquid fuel and oxidizer are introduced at the injection plate with known droplet sizes and mass flow rates. Part of fuel and oxidizer mass flow rates are considered as already vaporized and reacted at the inlet boundary, such that a mass flow rate of pre-existing gases is specified. At this inlet boundary, uniform initial conditions for velocity and temperature are given ($u_z = U_0, u_r = 0, T = T_0$). The inlet velocity U_0 is based on the given mass flow rate of pre-existing gases and combustion chamber cross-sectional area. The inlet gases temperature T_0 is computed as the equilibrium temperature of the combustion reaction for the given ratio of fuel to oxidizer mass flow rates $\dot{m}_f/\dot{m}_{ox}$.

At the chamber wall no slip boundary conditions and adiabatic wall are considered. At the centerline of the combustion chamber, symmetry conditions for the velocity components ($du_z/dr = 0, u_r = 0$) and adiabatic centerline condition for temperature ($dT/dr = 0$) are applied.

$$r = R \quad \rightarrow \quad u_z = u_r = \frac{dT}{dr} = 0, \tag{7}$$

$$r = 0 \quad \rightarrow \quad \frac{du_z}{dr} = u_r = \frac{dT}{dr} = 0. \tag{8}$$

Where R is the inner radius of the combustion chamber.

2.4 Solution procedure

The boundary layer equations presented above are solved numerically marching in the streamwise direction from given initial conditions. At each streamwise position, the boundary layer equations are solved numerically for the velocity and temperature distributions with a second order finite differences backward scheme in the streamwise direction and a second order centered finite differences scheme in the radial direction. The numerical model was developed in house and written in Fortran.

Second-order one-sided backward derivative in the streamwise direction

$$\frac{\partial u_z}{\partial z} \approx \frac{3u_z(i+1) - 4u_z(i) + u_z(i-1)}{2\Delta z}. \tag{9}$$

Where i stands for a given grid position in the streamwise direction $z(i)$.

Second order centered, first derivative in the radial direction

$$\frac{\partial u_z}{\partial r} \approx \frac{u_z(j+1) - u_z(j-1)}{2\Delta r}. \tag{10}$$

Where j stands for a given grid position in the radial direction, $r(j)$.

Second order centered, second derivative in the radial direction

$$\frac{\partial^2 u_z}{\partial r^2} \approx \frac{u_z(j+1) - 2u_z(j) + u_z(j-1)}{2\Delta r}. \tag{11}$$

The combustion gases composition and properties lag behind and are taken from the previous step $z(i)$ when marching to a new position $z(i+1)$.

Given the velocity and temperature fields at each computed streamwise position $z(i+1)$, the propellants evaporation is computed next and the following routine

computes the composition of the resulting combustion products. Liquid propellant evaporation is computed according to the methodology of [2] and [8]. The evaporation model considers the vaporization rate of a droplet $\dot{m}_d$ as a function of the thermal conductivity and specific heat at constant pressure of the propellant vapor phase (either for the fuel or oxidizer, and assuming Lewis number equal to unity), the droplet diameter D_d and the transfer number B_M.

$$\dot{m}_d = 2\pi D_d \frac{k}{c_p} \log(1 + B_M). \tag{12}$$

Where the transfer number is

$$B_M = \frac{Y}{1-Y}, \qquad Y = \left[1 + \left(\frac{p}{p_v} - 1\right)\frac{M_g}{M_p}\right]^{-1}. \tag{13}$$

Where Y is the propellant mass fraction, p_v is the vapor pressure of the propellant, M_p and M_g are the molar mass of the propellant and the molar mass of the surrounding high temperature ambient combustion gases.

The transfer number is valid for both steady and unsteady evaporation, when the drop temperature is increasing and heat from the hot gases are used both for increasing the droplet temperature and for evaporation. It is also assumed that the fuel mass fraction far from the droplet surface is equal to zero.

The properties necessary to compute the vaporization rate are evaluated at a reference temperature T_r, considering a mixture of combustion products and propellant vapor.

$$T_r = T_s + \frac{T - T_s}{3}. \tag{14}$$

Where T_s is the droplet temperature, which for the present model is assumed uniform.

$$Y_{\text{gas}} = 1 - \frac{2}{3}Y, \tag{15}$$

$$[c_p, k, \mu] = Y_{\text{gas}}[c_p, k, \mu]_{\text{gas}} + Y[c_p, k, \mu]_{\text{vapor}}, \tag{16}$$

$$\rho = \frac{Y_{\text{gas}}}{\rho_{\text{gas}}} + \frac{Y}{\rho_{\text{vapor}}}. \tag{17}$$

Thermodynamic and physical properties are computed based on correlations found on the National Institute of Standards and Technology (NIST) website (https://www.nist.gov/) and NASA Chemical Equilibrium Applications program (CEA) (https://cearun.grc.nasa.gov/).

Specific heat $\bar{c}_p$ and enthalpy $\bar{h}$ are evaluated from the following polynomials.

$$\frac{\bar{c}_p}{R_u} = a_1 + a_2 T + a_3 T^2 + a_4 T^3 + a_5 T^4, \tag{18}$$

$$\frac{\bar{h}}{R_u} = a_1 T + \frac{a_2 T^2}{2} + \frac{a_3 T^3}{3} + \frac{a_4 T^4}{4} + \frac{a_5 T^5}{5} + a_6. \tag{19}$$

The coefficients a_i for each one of the gases present on the combustion products are found on [11].

The resulting properties for the gas mixture are given by

$$\bar{c}_p = \sum_{i=1}^{N} X_i \bar{c}_{pi} \qquad \bar{h} = \sum_{i=1}^{N} X_i \bar{h}_i. \tag{20}$$

Physical properties result from kinetic theory for gases [7] and other sources [13, 18].

The viscosity coefficient for each species i is given by

$$\mu_i = \frac{5}{16\pi} \frac{\sqrt{\pi M_i / N_{av} k_B T}}{\sigma_i^2 \Omega^{(2,2)}}. \tag{21}$$

Where $N_{av} = 6.022e + 26$ 1/kmol is the Avogadro constant, $k_B = 1.3806e - 23$ is the Boltzmann constant, σ_i is the Lennard–Jones collision diameter and $\Omega^{(2,2)}$ is the collision integral.

The thermal conductivity coefficient for each species i is given by

$$k_i = \frac{\mu_i}{M_i}\left(f_{trans} c_v(trans) + f_{rot} c_v(rot) + f_{vib} c_v(vib)\right). \tag{22}$$

Where $c_v(trans)$, (rot) and (vib) are the molar specific heats due to translational, rotational and vibrational energies and

$$f_{trans} = \frac{5}{2}\left(1 - \frac{2}{\pi}\frac{c_v(rot)}{c_v(trans)}\frac{A}{B}\right),$$
$$f_{rot} = \frac{\rho_i D_{ii}}{\mu_i}\left(1 + \frac{2}{\pi}\frac{A}{B}\right),$$
$$f_{vib} = \frac{\rho_i D_{ii}}{\mu_i}.$$

With D_{ii} the auto-diffusion coefficient and A and B constants of the model.

$$c_v(trans) = \frac{3}{2}R_u,$$
$$c_v(rot) = c_v(vib) = 0 \quad \text{for simple atoms},$$
$$c_v(rot) = R_u, \quad c_v(vib) = c_v - \frac{5}{2}R_u, \quad \text{for linear molecules},$$
$$c_v(rot) = \frac{3}{2}R_u, \quad c_v(vib) = c_v - 3R_u, \quad \text{for nonlinear molecules}.$$

Chemical equilibrium conditions are determined for the reaction of UDMH and NTO. The combustion products are a mixture of the eleven species considered in the reaction: CO_2, CO, H_2O, H_2, O_2, N_2, H, OH, O, NO and N. The

properties of the mixture are evaluated according to the following rules.

$$\mu = \sum_{i=1}^{I} \frac{X_i \mu_i}{\sum_{j=1}^{J} X_j \Theta_{ij}},$$
$$\Theta_{ij} = \frac{1}{\sqrt{8}} \left(1 + \frac{\overline{M}_i}{\overline{M}_j}\right)^{-1/2} \left[1 + \left(\frac{\mu_i}{\mu_j}\right)^{1/2} \left(\frac{\overline{M}_j}{\overline{M}_i}\right)^{1/4}\right]^2. \quad (23)$$

$$k = \frac{1}{2}\left(\sum_{i=1}^{I} X_i k_i + \frac{1}{\sum_{i=1}^{I} X_i / k_i}\right). \quad (24)$$

Further details of the model for physical properties may be found on [7]. Liquid fuel and oxidizer propellant properties are evaluated from correlations taken from the NIST and NASA CEA, where correlations for vapor pressure based on Antoine equation and vaporization enthalpy are also available.

After the computation of the evaporation mass flow rates of fuel and oxidizer droplets, a chemical equilibrium routine is called to compute the composition of the products resulting from burning. Then, the pre-existing gases coming from $z(i)$ are mixed with the combustion products of the evaporated droplets at position $z(i+1)$ in a thermodynamic equilibrium and mass conservation routine to compute the mixture temperature, mass flow rate and gas velocity. Physical properties of the resulting gases are computed at the $z(i+1)$ station and another step in the streamwise direction is taken. The process is repeated until the fuel or oxidizer droplets are completely evaporated.

To start the computation the geometry of the combustion chamber, the fuel and oxidizer inlet areas and total mass flow rates are given, along with the liquid propellants temperature, combustion chamber pressure and amount of propellants already reacted at the chamber entrance. The gases resulting from the reaction at the chamber entrance simulate a recirculation zone of gases in the combustion chamber. The initial parameters will be presented in Sect. 2.6.

2.5 Verification and grid convergence tests

The boundary layer solver has been verified and validated against analytic results for inert flow on a channel. The inert incompressible flow on a constant area axisymmetric channel should evolve to a developed parabolic velocity profile downstream of the entry region. Figure 2 shows a comparison of the computed streamwise velocity radial distribution with the analytic parabolic velocity profile, showing good agreement. At the combustion chamber inlet a uniform velocity distribution was specified and marched downstream. At the end of the combustion chamber the velocity profile has evolved to the expected fully developed parabolic laminar velocity distribution.

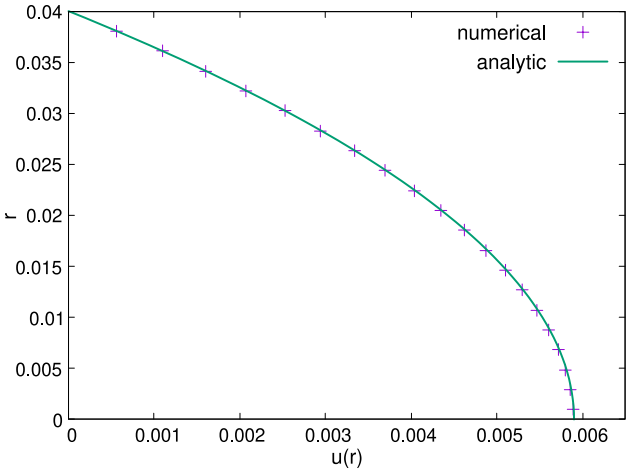

Fig. 2 Comparison between numerical velocity profile with analytic parabolic velocity profile

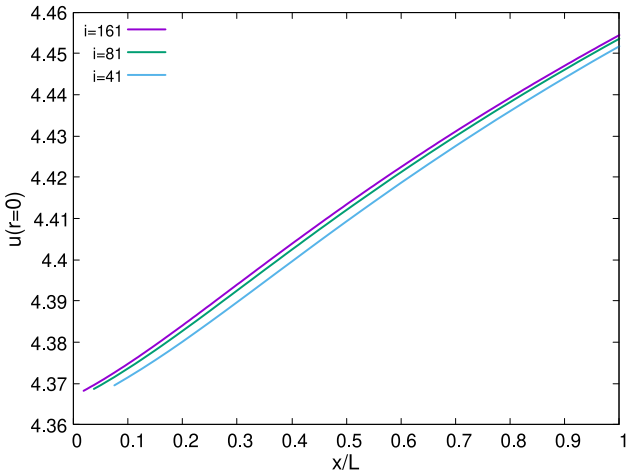

Fig. 3 Variation of the centerline velocity along the combustion chamber for three different grid points distributions

Figures 3 and 4 show the results of the grid refinement study. The grid refinement study is based on the simple technique of doubling the number of grid points and comparing results. A method such as the *Grid Convergence Index* could have been used, but for the structured grid used in the present study it would give results similar to the present results. In the streamwise direction, three values for the maximum number of grid points were tested, 41, 81 and 161. This choices of grid point quantities were based on previous experiences with the model. The difference in the centerline velocity at the end of the chamber is negligible and the difference in the velocity gradient at the chamber wall is of the order of 2% between the coarse grid and the fine grid.

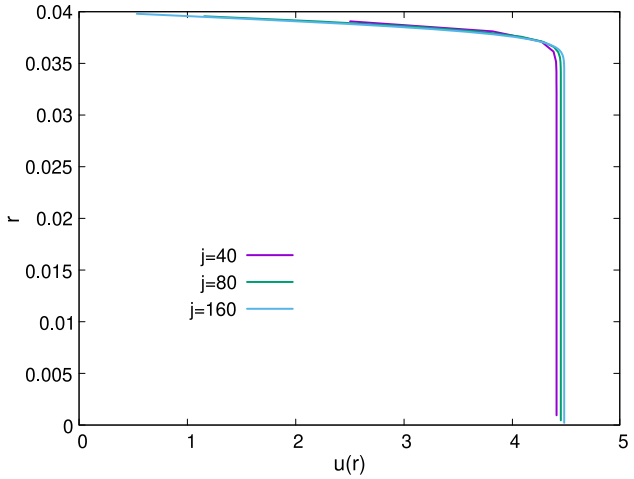

Fig. 4 Comparison of the radial velocity distribution at the end of the combustion chamber for three different grid points distributions

Figure 3 shows the variation of the centerline streamwise velocity $u(r = 0)$ along the streamwise direction for the three tested grid distributions.

Taken the number of grid points in the streamwise direction equal to 41, three different grid point distributions were tested in the radial direction, 40, 80 and 160 points. Again, the choice of grid points is based on previous experience with the model. Figures 4 show the streamwise velocity profile at the end of the chamber. The differences between the velocities for the three distributions of grid point is lower than 1%.

The size of the grid also has to be large enough to allow a minimum number of propellant droplets in each volume. Based on this requirement an on the grid refinement study, it was decided to use 41 grid points in the streamwise direction and 80 grid points in the radial direction.

The verification of the chemical equilibrium routine was performed comparing results with results obtained from NASA CEA. These results consider three different equivalence ratios, $\Phi = 0.2$, 1.0 and 5. Results are presented in Table 1 in terms of equilibrium temperature and product composition.

Finally, the droplets evaporation routine was validated considering the steady-state equilibrium droplet temperatures and the droplets vaporization rates. The test case considers a combustion chamber burning ethanol and hydrogen peroxide. Figure 5 shows the evolution of the fuel (T_f) and oxidizer (T_{ox}) droplets temperatures versus distance (x) along the combustion chamber. After an initial transient region, where the droplets are heated by the combustion gases at high temperatures, the droplets reach a steady state temperature close to the boiling temperature. For ethanol the boiling temperatures at 10 and 20 atmospheres are 425 and 454 K. For hydrogen peroxide they are 508 and 541 K. The corresponding steady state temperatures are $T_f(p = 10\ \text{atm}) = 415$ and $T_f(p = 20\ \text{atm}) = 445$ K for the ethanol and $T_{ox}(p = 10\ \text{atm}) = 497$ and $T_{ox}(p = 20\ \text{atm}) = 532$ for the

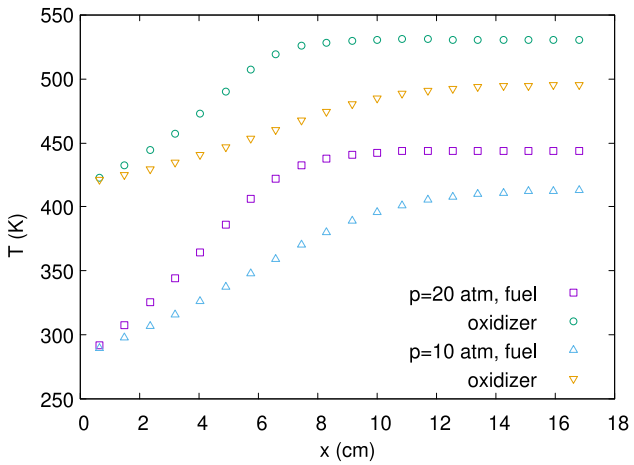

Fig. 5 Variation of the ethanol and hydrogen peroxide drop temperature along the combustion chamber for chamber pressures equal to 10 and 20 atm

Table 1 Results from the chemical equilibrium routine in terms of equilibrium temperature and composition for three different equivalence ratios

Equivalence ratio	0.2 Model	0.2 CEA	1 Model	1 CEA	5 Model	5 CEA
T [K]	3328	3325	3523	3520	2734	2733
M [g/mol]	20.89	20.89	18.95	18.95	13.94	13.94
$X(CO_2)$	0.02691	0.02675	0.0605	0.06014	0.0196	0.01944
X(CO)	0.01226	0.01242	0.0909	0.09132	0.3012	0.30134
$X(H_2O)$	0.5478	0.54679	0.5102	0.50956	0.2037	0.20384
$X(H_2)$	0.03142	0.03171	0.0929	0.09310	0.4645	0.46428
$X(O_2)$	0.2150	0.21471	0.0595	0.05962	2.5014E−6	< 1.E−5
X(H)	0.01537	0.01552	0.0421	0.04230	9.6658E−3	9.83E−3
X(OH)	0.1192	0.11961	0.1152	0.11540	1.2019E−3	1.25E−3
X(O)	0.03206	0.03209	0.0283	0.02835	1.4487E−5	2.00E−5

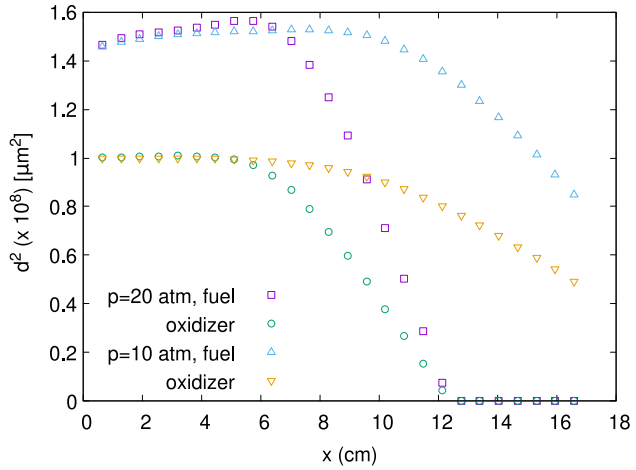

Fig. 6 Variation of the ethanol and hydrogen peroxide drop diameter squared along the combustion chamber for chamber pressures equal to 10 and 20 atm

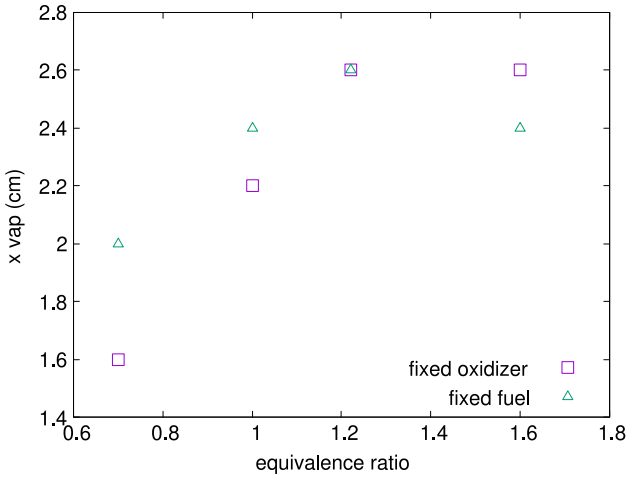

Fig. 7 Vaporization length x_{vap} (cm) versus initial equivalence ratio at the wall region. The equivalence ratio was changed either by changing the mass flow rate of the fuel and fixing the mass flow rate of the oxidizer, or vice-versa

hydrogen peroxide. These results are in agreement with the expected theoretic values [8].

In the steady-state regime the drop diameter should vary according to the diameter square law [8], which predicts that the square of the drop diameter should vary linearly downstream along the combustion chamber. Figure 6 shows the variation of the fuel (d_f) and oxidizer (d_{ox}) drop diameters squared, where after the unsteady drop warm up period the drop diameter squared varies linearly as expected. During the warm up period, the drops diameters do not vary significantly, since the reduction in diameter is compensated by an increase due to droplet dilatation with increasing temperature.

Table 2 Propellants mass flow rate, fuel/oxidizer equivalence ratio Φ, vaporization length x_v/L, core temperature and wall temperature at vaporization length x_v/L. Stoichiometric fuel/oxidizer ratio $f_s = 0.32658$. Fixed oxidizer mass flow rate for different fuel mass flow rates and fixed fuel mass flow rate for different oxidizer mass flow rates

Geometry and pressure					
$L = 80$ mm , $R = 40$ mm , $P = 20$ atm					
Fuel and oxidizer temperatures and inlet areas					
$T_f = 336$ K , $T_{ox} = 294$ K , $A_f = 15$ mm^2, $A_{ox} = 35$ mm^2					
total mass flow, fuel/oxidizer ratio and equivalence ratio					
$\dot{m}_f = 22 \times 10^{-3}$ kg/s , $\dot{m}_{ox} = 55 \times 10^{-3}$ kg/s , $f = 0.4$, $\Phi = 1.2248$					
core region					
$\dot{m}_f$ kg/s	$\dot{m}_{ox}$ kg/s	Φ	x/L_c(vap)		
13.86×10^{-3}	39.60×10^{-3}	1.22	0.325		
wall region fixed oxidizer mass flow for different fuel mass flow					
$\dot{m}_f$	$\dot{m}_{ox}$	Φ	x/L_c(vap)	$T(core)$ K	$T(wall)$ K
2.51×10^{-3}	$11. \times 10^{-3}$	0.70	0.200	2990	3076
3.59×10^{-3}		1.00	0.275	3017	3034
4.40×10^{-3}		1.22	0.325	3018	3022
5.75×10^{-3}		1.60	0.325	3018	2833
wall region fixed fuel mass flow for different oxidizer mass flow					
4.40×10^{-3}	19.25×10^{-3}	0.70	0.250	3011	3062
	13.47×10^{-3}	1.00	0.300	3020	3020
	11.04×10^{-3}	1.22	0.325	3018	3022
	8.42×10^{-3}	1.60	0.300	3020	2835

2.6 Combustion chamber parameters and operating conditions

The total fuel and oxidizer mass flow rates entering the combustion chamber $\dot{m}_f$, $\dot{m}_{ox}$, the resulting fuel to oxidizer mass flow ratio f and the equivalence ratio Φ are presented in Table 2. The combustion chamber length L_c, radius R and pressure P are also given in Table 2, along with the fuel and

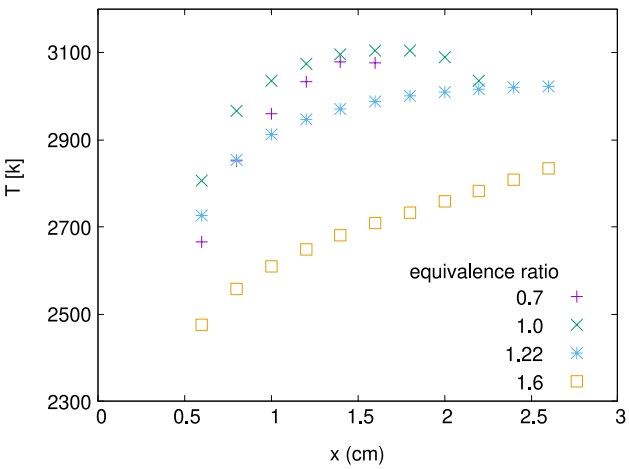

Fig. 8 Temperature variation along the chamber in the region close to the wall

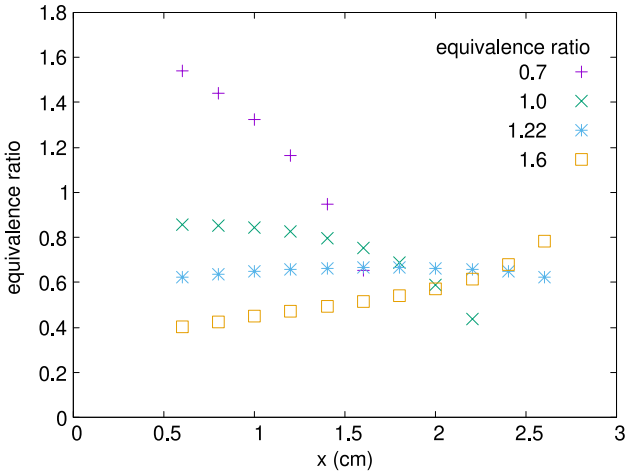

Fig. 9 Equivalence ratio variation along the chamber in the region close to the wall due to propellant evaporation

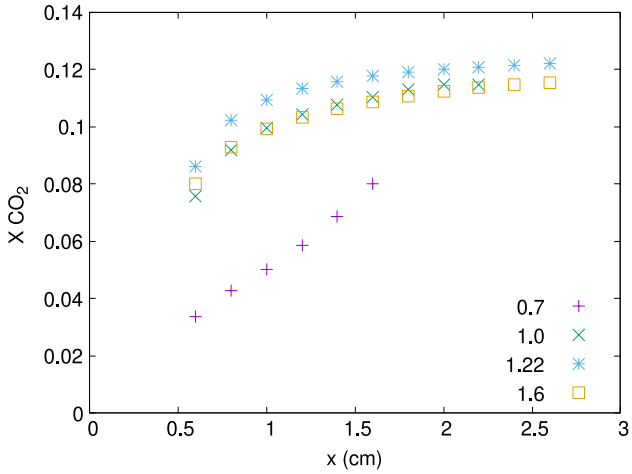

Fig. 10 CO_2 mole fraction along the chamber in the region close to the wall. $\Phi = 0.7$, 1, 1.22 and 1.66

oxidizer inlet temperatures, and injection areas, T_f, T_{ox}, A_f and A_{ox}, respectively.

In order to allow the definition of initial conditions to start marching the boundary layer equations, a percentage of the propellants is assumed to enter the combustion chamber and to evaporate and burn immediately. Physically, that would correspond to a combustion gases recirculation zone at the chamber entrance. The temperature of these pre-existing gases at the chamber entrance is determined according to the equilibrium temperature of fuel and oxidizer combustion at the specified chamber pressure. It was assumed that 10% of the oxidizer evaporate immediately at the entrance with a fuel/oxidizer ratio $f = 0.85$ for the initial evaporation of fuel. For the initial conditions considered, the resulting temperature of the pre-existing gases is equal to 2125 K. The code may be modified to used a user specified gas temperature and compute the resulting gas composition for the chosen mass fraction and temperature.

The condition $f = 0.4$, $\Phi = 1.2248$, at the inlet was taken as reference and the chamber was divided in two radial regions, a core region and a wall region. The core region takes 80% of the cross-sectional area and the wall region the remaining 20%. This choice of two distinct regions in the radial direction is meant to show the capability of the model in modeling a region close to the wall where lower temperature may be desirable. But the model would accept any radial distribution of equivalence ratio. The reference case is compared with three different cases where, in the wall region the inlet mass flow rates were taken such that the inlet equivalence ratio Φ are equal to 0.7, 1.0 and 1.6. The equivalence ratio for each one of these values were given either by changing the fuel mass flow rate or the oxidizer mass flow rate, but the results between the two options did not vary significantly for the evaporation length, wall temperature or chemical composition of the burned gases.

The inlet mass flow rates and fuel to oxidizer ratio for each test case is presented in Table 2. Also shown in Table 2 are the vaporization length (the length for total evaporation of either the fuel or oxidizer), the temperature at the center of the core region ($r = 0$) and the temperature at the wall at the streamwise position where one of the propellants has already totally evaporated.

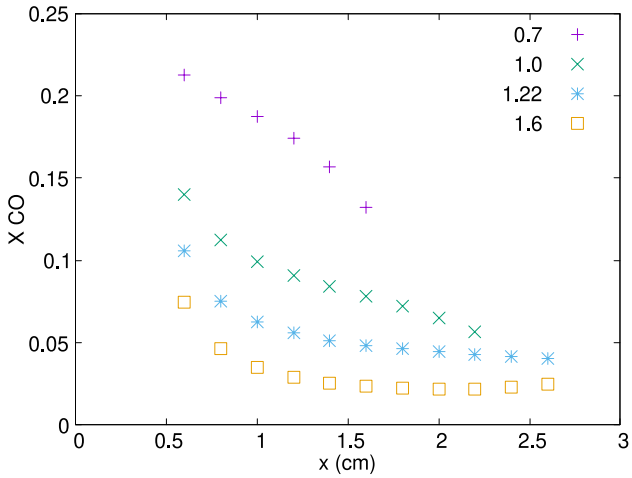

Fig. 11 *CO* mole fraction along the chamber in the region close to the wall. $\Phi = 0.7$, 1, 1.22 and 1.66

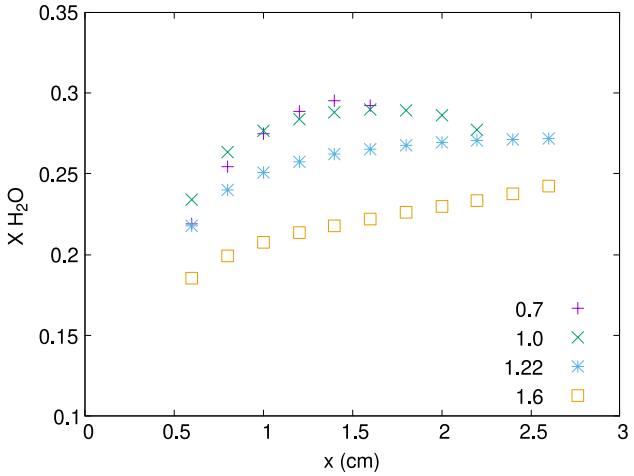

Fig. 12 H_2O mole fraction along the chamber in the region close to the wall. $\Phi = 0.7$, 1, 1.22 and 1.66

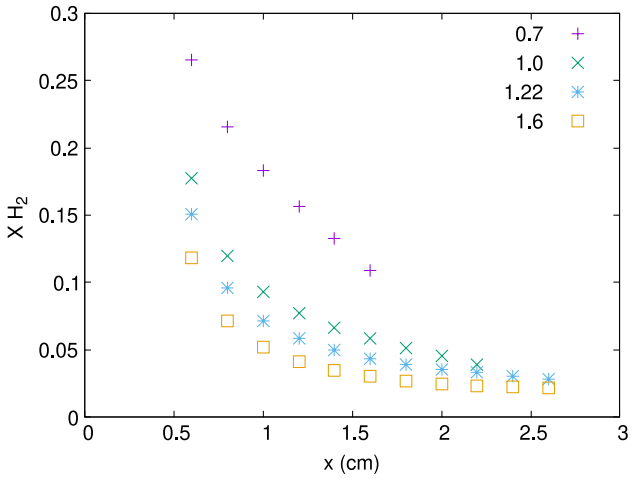

Fig. 13 H_2 mole fraction along the chamber in the region close to the wall. $\Phi = 0.7$, 1, 1.22, 1.66

3 Results

This section present results showing how the initial equivalence ratio and its radial variation affect the vaporization length, the temperature distribution along the chamber, the variation of the local equivalence ratio, the combustion gases composition, as well as velocity and the temperature distribution in the radial direction.

Figure 7 shows the vaporization length variation with initial equivalence ratio Φ. The vaporization length is relevant for sizing the combustion chamber and to assure that combustion is complete before the combustion gases enter the converging diverging nozzle. The initial equivalence ratios considered are those of: a) a uniform distribution with $\Phi = 1.2248$ and b) non-uniform distributions with $\Phi = 1.2248$ at the core region and $\Phi = 0.7, 1.0$ and 1.6 at wall region.

The equivalence ratio may increase due to a increase of the fuel mass flow rate or decrease of the oxidizer mass flow rate. As the equivalence rate increases the vaporization length also increases for $\Phi < 1.22$. For the lower values of Φ of 0.7 and 1.0, the fuel droplets evaporate first close to the wall and before the oxidizer droplets. For higher equivalence ratios ($\Phi = 1.6$), the fuel droplets evaporate also before the oxidizer, but first at the core region (where $\Phi = 1.22$). If the initial equivalence ratio is changed by fixing the fuel mass flow rate and changing the oxidizer mass flow rate, the fuel droplets evaporate before the oxidizer at the core region, except for $\Phi = 1.6$ when the oxidizer at the wall region evaporates first. This is because at $\Phi = 1.6$ the mass flow rate of the oxidizer is considerably lower and the vaporization length drops to $x/L_c = 0.30$.

The vaporization length is a function of the combustion gases temperature, which increases for equivalence ratios between 1 and 1.2. Higher temperatures would lead to faster evaporation, but the vaporization length is also a function of the droplets velocities, which change when mass flow rates are changed. Higher droplet velocity results in lower residence time in a give control volume of length Δx along the chamber. The vaporization length is also a function of the local equivalence ratios, given by the relation between fuel and oxidizer evaporated masses.

Figure 8 shows the variation downstream of the temperature close to the chamber wall for different values of the initial equivalence ratio. For $\Phi = 0.7$ the gas temperature increases as the equivalence ratio due to evaporation decreases toward one along the chamber due to propellants evaporation. The initial pre-existing gases at 2125 K mixes with combustion gas increasing the total temperature in the chamber. As the local equivalence ratio decreases downstream due to different evaporation rates of fuel and oxidizer, the gas temperature continues to increase. Increasing the initial equivalence ratio to $\Phi = 1.0$, increases the wall temperature. Higher initial equivalence ratios ($\Phi = 1.22$ and $\Phi = 1.6$) result in lower temperatures compared to $\Phi = 1.0$.

There is a strong correlation between the gas temperature and the local equivalence ratio. Given an initial equivalence ratio at the chamber inlet, the evaporation of droplets along the chamber results in a streamwise variation of the local equivalence ratio, as shown in Fig 9. These downstream equivalence ratios correspond to the ratios between evaporated fuel and oxidizer. Figure 9 shows that the resulting local equivalence ratio due to evaporation varies significantly due to fuel evaporation when excess oxidizer is considered at the inlet ($\Phi = .7$). In this case, the local equivalence ratio due to evaporation drops from about 1.6 to values close to the stoichiometric condition ($\Phi = 1$). This drop in

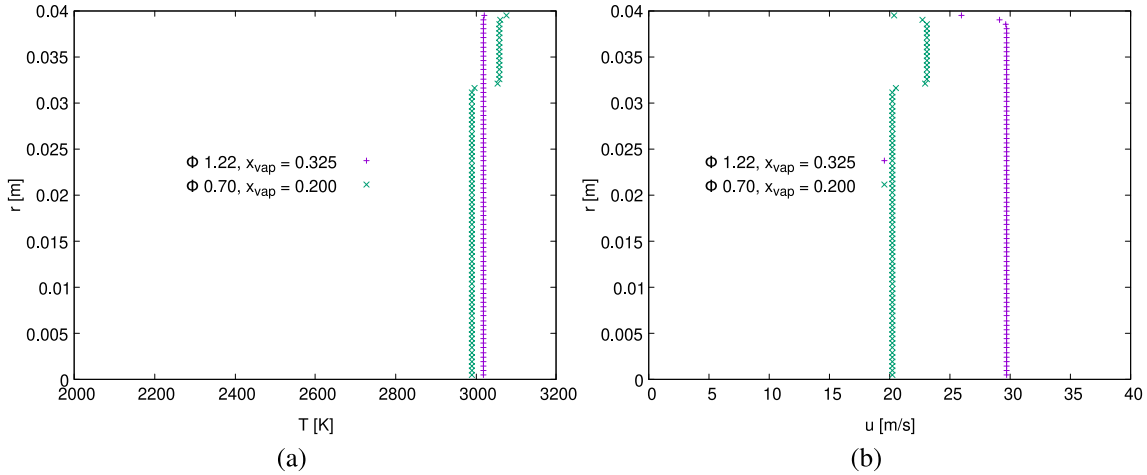

Fig. 14 Temperature and velocity profiles at the position x_{vap} for $\Phi = 0.70$ in the wall region

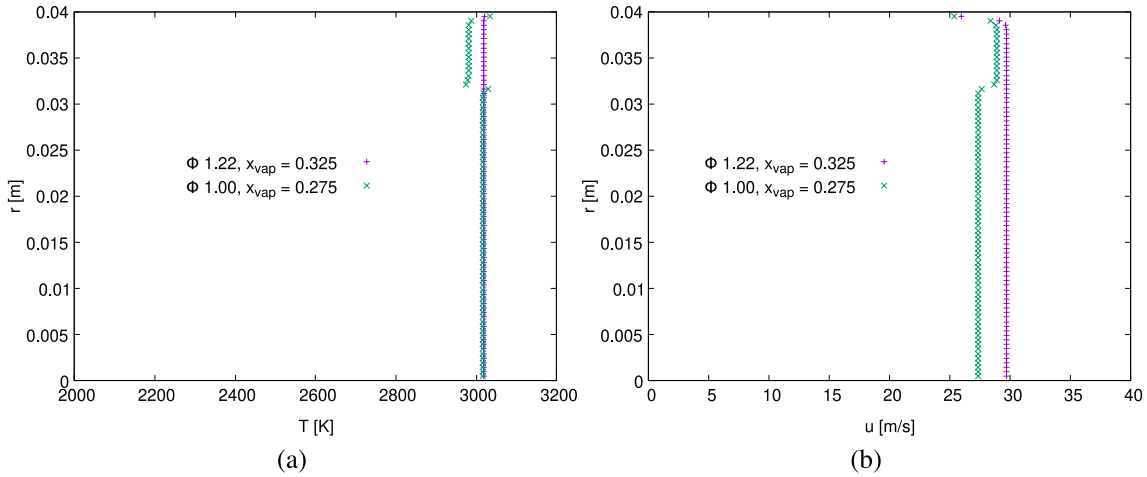

Fig. 15 Temperature and velocity profiles at the position x_{vap} for $\Phi = 1.0$ in the wall region

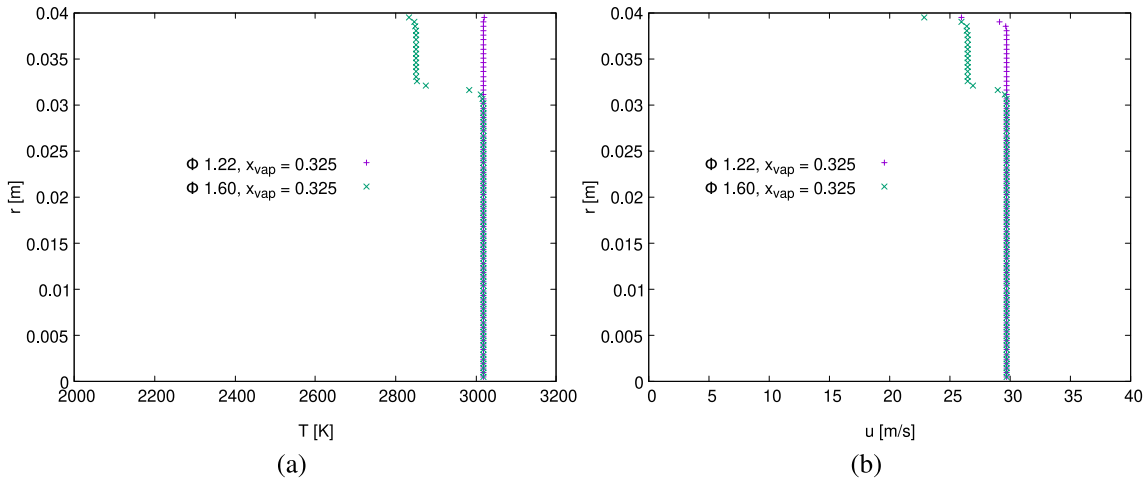

Fig. 16 Temperature and velocity profiles at the position x_{vap} for $\Phi = 1.6$ in the wall region

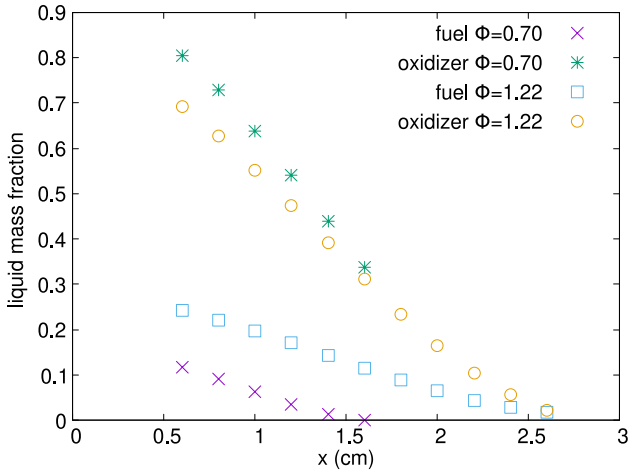

Fig. 17 Liquid mass fraction variation along the combustion chamber both at the core and wall regions for initial equivalence ratio $\Phi = 0.7$ at the wall region

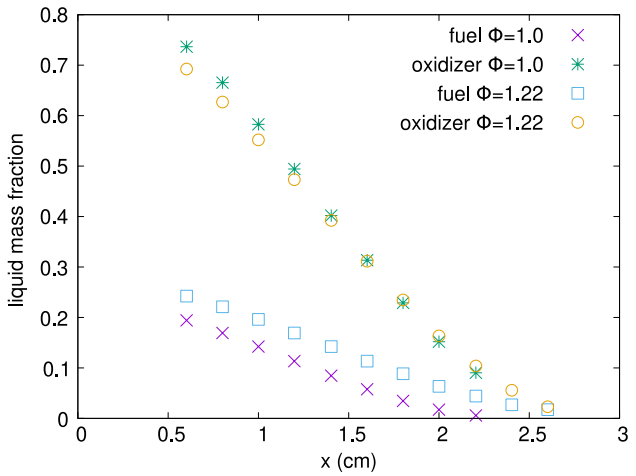

Fig. 18 Liquid mass fraction variation along the combustion chamber both at the core and wall regions for initial equivalence ratio $\Phi = 1.0$ at the wall region

the local equivalence ratio results in an increase in gas temperature as shown in Fig. 8. For the other initial equivalence ratios ($\Phi = 1.0$, 1.22 and 1.6) the streamwise variation of Φ are not so strong and the resulting gas temperature close to the wall increases as Φ tends to the stoichiometric condition or decreases when it varies away from stoichiometry. Keep in mind that the temperature close to the inlet is influenced by the pre-existing gas temperature of 2125 K.

Mole fraction variation along the length of the chamber in the wall region for CO_2, CO, H_2O and H_2 are shown in Figs. 10, 11, 12 and 13. Significant increase in CO_2 is observed for equivalence ratios higher than 0.7 due to a higher percentage of fuel in the evaporated mixture as shown

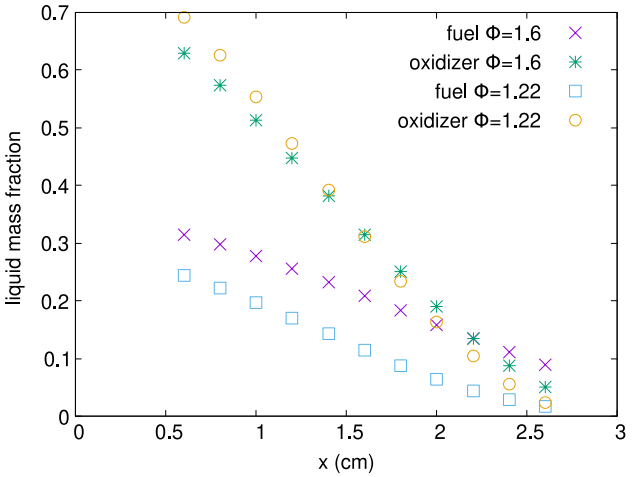

Fig. 19 Liquid mass fraction variation along the combustion chamber both at the core and wall regions for initial equivalence ratio $\Phi = 1.6$ at the wall region

in Fig. 9. Mole fractions of CO, and H_2 decrease downstream with increasing inlet equivalence ratio, following an opposite trend than that of CO_2. Downstream, the predominant gases are CO_2 and H_2O, since the equivalence ratio are closer to the stoichiometric value.

Next, temperature and velocity profiles in the radial direction ($T(r)$,$u(r)$) are presented in Figs. 14, 15 and 16. The profiles are taken at the streamwise position where the droplets have totally evaporated for each equivalence ratio. Each plot shows profiles for each equivalence ratio as well as profiles for the reference case, where the equivalence ratio of $\Phi = 1.2248$ was imposed both at the core and wall regions.

As shown in Fig. 8, the wall temperature is higher when the equivalence ratio is close to one. Given the adiabatic boundary condition at the wall and the combustion reaction in the region close to the wall, the resulting temperature distribution shown in Figs. 14a, 15a and 16a is mostly uniform. The wall temperature depends on the wall region reaction, and the resulting thermal boundary layer is very thin. This same result about the boundary layer thickness is also valid for the velocity profile, where the reaction of the evaporated propellants increase the mass flow rate of gases close to the wall and prevent the development of a thick boundary layer as seen in Figs. 14(b), 15(b) and 16(b). As a consequence, the temperatures near the wall are high along the chamber, demanding wall cooling or intermittent chamber operation in short burst to allow time for wall cooling. Comparison between different equivalence ratio results depends also on the vaporization length of each case, so that profiles are not compared at the same streamwise position. Nevertheless, the effect of

equivalence ratio variation from the core region to the wall region is clearly shown.

The temperature plots show that the wall region is not sufficiently resolved. This is because the grid spacing cannot be strongly refined or there will not be enough propellant droplets in the resulting small volume. At each grid control volume the number of droplets is proportional to the mass flow at that volume which cannot be made to small. Given that the boundary layer thickness is very thin due to the constant addition of gas mass flow from the burning of evaporated propellants, there is a balance between grid refinement to capture the boundary layer and grid spacing to allow a minimum number of droplets in the wall region.

To further understand the local equivalence ratio variation downstream, Figs. 17, 18 and 19 show the fuel and oxidizer liquid mass fraction ratio for initial equivalence ratios $\Phi = 0.70$, 1.0 and 1.6, respectively. The different values of equivalence ratio for these test cases correspond to a given mass flow rate of oxidizer and increasing mass flow rates of fuel at the wall region, corresponding to the first group of conditions in Table 2.

The mass fraction ratio in these plots is defined as the ratio between the liquid mass at a streamwise station x and the total, fuel plus oxidizer, initial liquid mass at the chamber inlet at $x = 0$. Each plot also shows the reference case $\Phi = 1.2248$ where the equivalence ratio is uniform across the radial direction, both in the core and wall regions. All three plots show that, for any value of the initial equivalence ratio Φ the oxidizer is consumed at a greater rate than the fuel, but since the amount of injected fuel is lower than that of the oxidizer, the fuel is completely consumed shortly before the oxidizer.

For $\Phi = 0.7$, Fig. 17 shows that the fuel evaporates completely in the region close to the wall before the oxidizer. There is a considerable amount of remaining liquid oxidizer after the fuel has completely evaporated. The higher evaporation rate of oxidizer reduces the equivalence ratio downstream, as shown in Fig. 9, increasing the gas temperature, as shown in Fig. 8.

For the equivalence ratio of $\Phi = 1.0$, shown in Fig. 18, the trend is the same, but due to the higher initial amount of fuel, the fuel takes longer to fully evaporate and a greater quantity of oxidizer is consumed. On the other hand, for $\Phi = 1.6$ (18), fuel and oxidizer are fully consumed at about the same streamwise position at the core region first, with remaining liquid propellants at the wall region. This is due to the greater amount of fuel at the wall region.

The increase in the local equivalence ratio for initial $\Phi = 1.6$, shown in Fig. 9 is due to the greater fuel mass flow shown in Fig. 19, which results in higher number of fuel droplets and, therefore, higher evaporated mass of fuel with respect to the evaporated mass of oxidizer. This is correlated with the velocity plots shown in Fig. 16, where less quantity of burned gases result in lower velocities close to the wall, while for $\Phi = 0.70$ and 1.0, greater evaporation close to the wall result in higher velocities than that observed in the core region (Figs. 14 and 15).

4 Conclusions

A new 2D numerical model, based on the boundary layer equations, was developed for simulation of spray combustion along an axisymmetric combustion chamber. The present model allows the analysis of different operation conditions and the fast determination of evaporation lengths, heat transfer to the chamber walls, composition of reactants and products, temperatures, velocities, densities, droplet sizes and other important parameters which are required for the design of rocket combustion chambers. Consequently, design cost and time can be reduced, as well as the number of tests of prototypes.

Different equivalence ratio distributions were considered in order to reduce the gas temperature near the chamber wall. Evaporation lengths were calculated in different operating conditions in order to determine the combustion chamber length. The results indicate that the evaporation length is a function of combustion gases temperature, which depends on the initial equivalence ratio as well as on the local equivalence ratio given by fuel and oxidizer evaporation rates. The evaporation length also depends on the fuel and oxidizer mass flow rates, which sets the droplets speeds through the chamber.

In agreement with previous published results, the present results also show that the boundary layer thickness is very thin due to the constant addition of heat and mass flow close to the wall from combustion and that the near wall temperature depends on the equivalence ratio. As a consequence, large heat transfer to the walls is expected and either the walls must be cooled or the chamber should be only run for short burst periods.

The model is currently under development and further refinements will be incorporated, such as conjugate heat transfer between the combustion gases and the chamber walls, to account for wall cooling and heat losses through the walls; multiple droplet sizes based on the Rosin-Rammler distribution functions; and analysis of other propellants, specially green propellants, such as ethanol and hydrogen peroxide.

Acknowledgements The author acknowledges the financial support from CAPES (Coordenadoria de Aperfeiçoamento de Pessoal de Nível Superior) and CNPq (Conselho Nacional de Desenvolvimento Científico e Tecnológico). Both financial supports are grants from Government institutions related to higher education and public research funding. The authors have no Conflict of interest to declare that are relevant to the content of this article. The authors are solely responsible for the printed material included in this paper.

References

1. Cheng GC, Farmer R (2006) Real fluid modeling of multiphase flows in liquid rocket engine combustors. J Propul Power 22(6):1373–1381
2. Chin JS, Lefebvre AH (1983) Steady-state evaporation characteristics of hydrocarbon fuel drops. AIAA J 21(10):1437–1443
3. Haidn OJ (2001) 2nd international workshop on rocket combustion modeling. DLR and European Office of Aerospace Research and Development, DLR, Langer Grund Lampoldshausen, Germany
4. Kalmykov GP, Larionov AA, Sidlerov DA, Yanchilin LA (2009) Numerical simulation of operation processes in the combustion chamber and gas generator of oxygen-methane liquid rocket engine. Prog Propul Phys 1:185–204
5. Kang YD, Sun B (2011) Numerical simulation of liquid rocket engine thrust chamber regenerative cooling. J Thermophys Heat Transf 25(1):155–164
6. Kuo KK (1986) Principles of combustion. Wiley-Interscience. Wiley, New York
7. Law CK (2006) Combustion physics. Cambridge University Press, Cambridge
8. Lefebvre AH, McDonell VG (2017) Atomization and sprays, 2nd edn. CRC Press, Boca Raton
9. Maya E, Valdes J (2018) Numerical modeling of combustion process in hybrid rocket engines using open source software. American Institute of Aeronautics and Astronautics, AIAA, Ohio, USA, AIAA paper 2018-4438
10. Mazzeti A, Barbante P (2016) Numerical modeling of combustion processes in hybrid rocket engines. Int J Energetic Mater Chem Propul 15(3):249–2746. https://doi.org/10.1615/IntJEnergeticMaterialsChemProp.2016013641
11. McBride BJ, Gordon S, Reno MA (1993) Coefficients for calculating thermodynamic and transport properties of individual species. Reference publication 4513, National Aeronautics and Space Administration, National Aeronautics and Space Administration. Lewis Research Center. Cleveland, Ohio 44135
12. Oefelein JC, Yang V (1998) Modeling high-pressure mixing and combustion processes in liquid rocket engines. J Propul Power 14(5):843–857
13. Poling BE, Prausnitz JH, O'Connell JP (1977) The properties of gases and liquids, 5th edn. McGraw-Hill, New York
14. Raman V, Hassanaly M (2019) Emerging trends in numerical simulations of combustion systems. Proc Combust Inst 37(2):2073–2089
15. Riedmann H, Banuti D, Ivancic B, Knab O, Hannemann K (2019) Modeling of h2/o2 single-element rocket thrust chamber combustion at sub- and supercritical pressures with different computational fluid dynamics tools. Prog Propul Phys 11:247–272
16. Salvador CAV, Costa FS (2006) Vaporization lengths of hydrazine fuels burning wih nto. J Propul Power 22(6):1362–1372
17. Salvador NM, Mendonca MT, Dourado WMC (2013) Large eddy simulation of bluff body stabilized turbulent premixed flame. J Aerosp Technol Manag 5(2):181–196
18. Svehla RA (1995) Transport coefficients for the Nasa Lewis chemical equilibrium program. Technical Memorandum 4647, NASA, National Aeronautics and Space Administration. Lewis Research Center. Cleveland, Ohio 44135
19. Xu J, Jin P, Li R, Wang J, Cai G (2020) Effect of coaxial injector parameters on lox/methane engines: a numerical analysis. Acta Astronaut 171:225–237